Chinese Chemical Letters 37 (2026) 112313

Contents lists available at ScienceDirect

Chinese Chemical Letters

journal homepage: www.elsevier.com/locate/cclet

Unveiling the enhanced activity origin of $BiO_{1-x}Cl/C_3N_5$ photocatalyst in CO_2-to-CO directional conversion

Zhilei Chen[a], Zhaoxia Li[a], Yunjiang Yu[b], Mingdeng Xiang[b], Cheng Ding[a,*], Entian Cui[a], Jizhou Jiang[c,d,*]

[a] School of Environmental Science and Engineering, Key Laboratory for Advanced Technology in Environmental Protection of Jiangsu Province, Yancheng Institute of Technology Yancheng, Yancheng 224051, China
[b] Key Laboratory of Environmental Pollution Health Risk Assessment, Ministry of Ecology and Environment of the People's Republic of China, South China Institute of Environmental sciences, Guangzhou 510655, China
[c] School of Materials Science and Engineering, State Key Laboratory of Green and Efficient Development of Phosphorus Resources, Engineering Research Center of Phosphorus Resources Development and Utilization of Ministry of Education, Key Laboratory of Green Chemical Engineering Process of Ministry of Education, Hubei Key Laboratory of Plasma Chemistry and Advanced Materials, Novel Catalytic Materials of Hubei Engineering Research Center, Wuhan Institute of Technology, Wuhan 430205, China
[d] College of Chemistry and Molecular Sciences, Wuhan University, Wuhan 430072, China

ARTICLE INFO

Article history:
Received 22 October 2025
Revised 8 December 2025
Accepted 22 December 2025
Available online 22 December 2025

Keywords:
Photocatalysis
CO_2 reduction
Composite catalyst
Structure dynamic evolution
In-situ characterization

ABSTRACT

The structure of photocatalysts largely determines the selectivity of CO_2 conversion products in CO_2 photoreduction reaction, while it is dynamic during the photoreaction. Therefore, how the dynamic structure affecting photoactivity deserves further investigation. Herein, with defective oxygen vacancies $BiOCl/C_3N_5$ nanosheets heterojunction ($BiO_{1-x}Cl/C_3N_5$) as model photocatalyst, the structure dynamic evolution in CO_2 photoreduction reaction and its influence on the CO_2-to-CO directional conversion were investigated. Specially, in $BiO_{1-x}Cl/C_3N_5$, the exposed Bi atoms adjected oxygen vacancies interacted with N atoms of C_3N_5 *via* the strong electrostatic effect, resulting in the shrinking crystalline structures. Once illuminated, the photogenerated electrons enriched on Bi active sites, which further strengthened the interfacial interaction between $BiO_{1-x}Cl$ and C_3N_5 to a *quasi*-bonding state. The resulting changes in electronic structure destroyed the linear structure of CO_2 molecule pre-adsorbed on Bi sites, accompanying with transformation of Bi atom valence states and heterostructure restoration. As a result, the $^*CO_2$ molecule activation and $^*CO$ intermediate desorption barrier energies both reduced, promoting the CO_2-to-CO directional conversion with a CO evolution rate of 207.3 $\mu mol\ g^{-1}\ h^{-1}$. This work demonstrated the importance of studying the structural dynamics evolution in photoreactions, which may be beneficial for future photocatalyst design.

© 2026 Published by Elsevier B.V. on behalf of Chinese Chemical Society and Institute of Materia Medica, Chinese Academy of Medical Sciences.

Solar-driven CO_2 reduction now is a promising technology to solve the environmental problem and energy crisis [1,2]. The carbon-contained products were various, and among them, carbon monoxide (CO) is a momentous constituent for bulk chemical manufacturing. Therefore, the photocatalytic CO_2-to-CO conversion with high activity and selectivity is highly sought after. However, the dissociation energy of the C=O bond in CO_2 molecules is as high as 750 kJ/mol, which makes the CO_2 photoreduction an arduous reaction [3,4]. Up to now, the reported CO yields and selectivity in CO_2 photoreduction reaction were relatively low [5,6], which greatly restricted the application of solar-driven CO_2 reduction technology. Seeking a high-performance photocatalyst for CO_2-to-CO directional conversion is the hotspot and difficulty in the photocatalytic field.

Recently, bismuth-based materials, such as Bi_2O_3 [7,8], BiOBr [9,10], $BiOI_3$ [11,12], and BiOCl [13,14], have been proved to be promising photocatalysts for their unique electronic structures and layered crystal structures. Among them, BiOCl has received widespread attention [15–17]. However, its solar-to-fuel efficiency is restricted greatly by its wide band gap. Various strategies have been tried to improve the photocatalytic activity of BiOCl, such as exposed facets regulation [18–20], heterojunction configuration [21,22], (non)metal doping [23,24], and so on. Recently, studies have suggested that introducing oxygen vacancies in heterojunction structure can efficiently promote the photocatalytic performance [25–27]. Nevertheless, despite considerable efforts devoted

* Corresponding authors.
E-mail addresses: ycdingc@163.com (C. Ding), 027wit@163.com (J. Jiang).

https://doi.org/10.1016/j.cclet.2025.112313
1001-8417/© 2026 Published by Elsevier B.V. on behalf of Chinese Chemical Society and Institute of Materia Medica, Chinese Academy of Medical Sciences.

to improving the performances of BiOCl-based heterojunction photocatalysts, the intrinsic mechanisms currently remain ambiguous.

In CO_2 photoreduction reaction, the ultimate photocatalytic performance is a result of multiple factors working together, such as the photocarrier-separation efficiency, the adsorption type of CO_2 molecules, the activation energy of CO_2 molecules, and the $^*CO$ intermediates formation energy. Studies have shown that affected by the reaction environment, the surface structure and interface structure of photocatalysts were dynamically changing [28,29], which caused the changes in surface atomic configuration, electronic structure, and spatial distribution of active sites. For instance, by the selective photo-deposition of PtO_x species on $BiOIO_3$ surface, under light irradiation, the surface adsorbed CO_2 molecules transformed into $^*CO$ intermediates, leading to the emergence of Bi^{3+} species and the expansion of crystalline structure of $BiOIO_3$ nanocrystals [12]. Furthermore, the Pt_1-$ZnIn_2S_4$@CoO_x system underwent a hole-induced oxidative self-reconstruction of CoO_x, which continuously scavenged photogenerated holes and effectively suppressed photocorrosion. Consequently, it achieved hydrogen evolution rates of 23.88 mmol g^{-1} h^{-1} in natural seawater and 48.99 mmol g^{-1} h^{-1} in deionized water [30]. Therefore, investigating the dynamic evolutions of crystal structure of BiOCl-based materials in CO_2 photoreduction process and its fluence on the photocatalytic activity is a reasonable way to explore the essence of CO_2 photoreduction reaction, which is also beneficial for the rational designs of efficient CO_2 reduction photocatalysts.

Herein, by adopting *quasi in-situ* characterization techniques, we explored the dynamic structure and chemical-state variations on $BiO_{1-x}Cl/C_3N_5$ in CO_2 photoreduction process with $BiO_{1-x}Cl$ and $BiOCl/C_3N_5$ counterparts for comparison. The related studies clearly revealed that in $BiO_{1-X}Cl/C_3N_5$, electron offset could efficiently be promoted from interfacial N atoms to Bi atoms, inducing intimate interface contact and strengthening the adsorption of CO_2 molecules. It resulted in the low oxidation state Bi atoms and the local contraction of $BiO_{1-x}Cl$ structures. Under light irradiation, the interface interaction was further enhanced, which promoted the activation of CO_2 molecule and the interfacial electron transport. Owing to the photoinduced electrons enrichment on interface Bi sites, the adsorbed CO_2 molecules were transformed into $^*CO$ intermediates with the expansion of crystalline structures. As expected, $BiO_{1-x}Cl/C_3N_5$ exhibited the highest CO_2-to-CO conversion performance in comparison to $BiO_{1-x}Cl$ and $BiOCl/C_3N_5$. These findings might provide a feasible strategy to elucidate the dynamic evolution process of catalytically active sites for the significantly enhanced CO_2-to-CO directional conversion, which offers new insights for the fabrication of highly efficient CO_2 photo-reduction catalysts.

$BiO_{1-x}Cl$ was prepared *via* a simple hydrothermal process [31]. $Bi(NO_3)_3{\cdot}5H_2O$ (1 g) was first dissolved in 25 mL of ethylene glycol and stirred for 30 min to ensure the complete dissolution. After that, 5 mL of saturated NaCl solution was added. After stirring for another 60 min, the mixture was transferred into a 100 mL hydrothermal autoclave and kept at 160 °C for 5 h. The $BiO_{1-x}Cl$ product was collected after washing, centrifugation, and freeze-dried treatment.

5-Amino-1,2,4-triazole (5 g) and NH_4Cl (5 g) were milled to form an inhomogeneous solid mixture and then was treated at 550 °C for 3 h with a heating rate of 10 °C/min. The product was naturally cooled and the obtained sample was bulk C_3N_5.

Bulk C_3N_5 (1 g) was processed into 40 mL of concentrated H_2SO_4 with continuous stirring for 12 h. The yellowish product was washed to neutral by deionized water and then dried under vacuum at 60 °C for 12 h.

The synthesis procedure of $BiO_{1-x}Cl/C_3N_5$ was similar to that of $BiO_{1-x}Cl$, except a certain amount of prepared C_3N_5 nanosheets was injected into the mixture solution of $Bi(NO_3)_3{\cdot}5H_2O$ and ethylene glycol.

Sample morphology was measured by transmission electron microscopy (TEM, FEI Tecnai TF20). XRD pattern was collected by X'Pert PRO, PANalytical with a scanning rate of 0.06°/s. The chemical valence and elemental composition of the catalyst surface were determined by ESCALAB 250 Xi X-ray photoelectron spectroscopy. UV–vis diffuse reflectance spectra were characterized on a UV-2550 (Shimadzu) spectrometer. Both steady and time-resolved Photoluminescence (PL) spectra were recorded on Fluorescence Spectrophotometer F-7000 and HORIBA FL-3, respectively. EPR measurements were recorded using Bruker EMX nano.

The synchronous irradiation X-ray diffraction (SI-XRD) was performed using a 300 W xenon lamp as the light source to record XRD data before and after CO_2 adsorption as well as light irradiation. The CO_2-preadsorption process was presented in Fig. S1 (Supporting information). Specially, after being made into thin sheets with suitable size, the photocatalyst was placed in a sealed adsorption chamber and purged with Ar (50 mL/min) for 30 min to remove the surface adsorbed impurities. Subsequently, a mixture gas of CO_2 and water vapor was introduced into adsorption chamber for 60 min. Finally, the import valve and export valve of sealed chamber were closed and kept it for 60 min at room temperature to reach the adsorption equilibrium.

In-situ diffuse reflectance Fourier transform infrared spectroscopy (SI-DRIFTS) was carried out on a Bruker VERTEX 70 infrared spectrometer with a 300 W Xe lamp (PLS-SXE300, Perfectlight Technology Co, Ltd., Beijing) as light source. A mixed atmosphere ($CO_2 + H_2O$ vapor) was injected into the reactor for 30 min at room temperature. After reaching the sorption equilibrium, SI-DRIFTS data were recorded under alternating dark and light conditions.

Synchronous irradiation X-ray photoelectron spectroscopy (SI-XPS): The synchronous irradiation X-ray photoelectron spectroscopy (SI-XPS) instrument was equipped with a 300 W Xe lamp as light source. Before SI-XPS measurements, after being made into thin sheets with suitable size, the photocatalyst was placed in a sealed adsorption chamber and purged with Ar (50 mL/min) at 120 °C for 30 min to remove the surface adsorbed impurities. Subsequently, a CO_2/H_2O (vapor) was purged into the chamber at room temperature for 20 min to reach the adsorption equilibrium. Finally, the as-prepared samples were quickly transferred to the analysis chamber of XPS instrument (ESCALAB 250Xi) for the SI-XPS measurements. The variations of XPS spectra were recorded by controlling light irradiation (on or off). The CO_2-preadsorption process was presented in Fig. S1.

The photocatalytic CO_2 reduction activity was carried out under the irradiation of 300 W Xe lamp (PLS-SXE300, Perfectlight Technology Co, Ltd., Beijing) equipped with a 420 nm cutoff filter (Perfect Light, Microsolar 300, 420–780 nm). In a typical reaction, 100 mg samples were dispersed uniformly in pure water. The hybrid suspension was then transferred into the tailor-made vessel. Before irradiation, ultrahigh purity CO_2 (99.999 %) gas was bubbled into the suspension at 300 mL/min for 30 min to remove air and saturate the solution. The reactor temperature was kept at 25 °C with a cooling water circulator. After 5 h magnetic stirring under light irradiation, the suspension was centrifuged to collect the catalyst. The products were analyzed using Agilent GC 6890 N gas chromatograph with thermal conductivity and flame ionization detectors.

For comparison, the CO_2 photoreduction performance with sacrificial reagent MeCN addition was also carried out. The testing procedure was similar with MeCN solution replacing pure water.

In isotopic labeling experiment, $^{13}CO_2$ gas was employed instead of $^{12}CO_2$ gas as the carbon source, and $H_2{}^{18}O$ was utilized

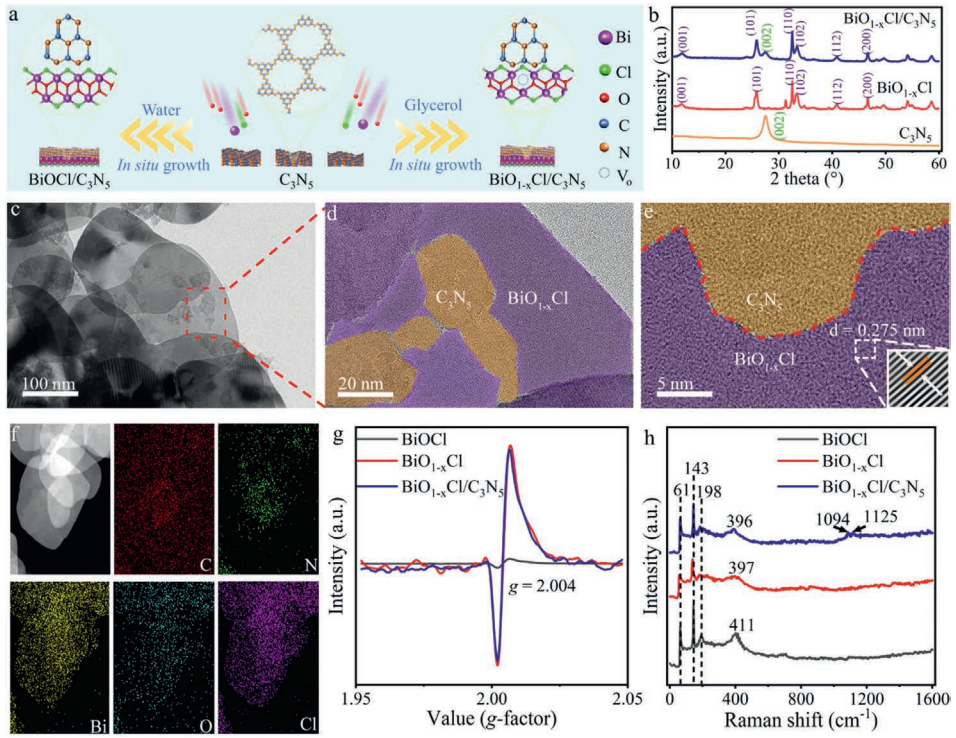


Fig. 1. (a) The synthetic procedure of $BiO_{1-x}Cl/C_3N_5$. (b) XRD, (c-e) TEM, and HRTEM of $BiO_{1-x}Cl/C_3N_5$. (f) Elemental mapping images of $BiO_{1-x}Cl/C_3N_5$. (g) Electron paramagnetic resonance spectra (EPR) of BiOCl, $BiO_{1-x}Cl$, and $BiO_{1-x}Cl/C_3N_5$. (h) Raman spectra of BiOCl, $BiO_{1-x}Cl$, and $BiO_{1-x}Cl/C_3N_5$.

instead of $H_2{}^{16}O$. The gas products were measured by GC–MS spectrometry.

The photoelectrochemical data were all measured by a three-electrode photoelectrochemical cell with sample photoelectrode as working electrode, Pt sheet as counter electrode, and Ag/AgCl as reference electrode. Additionally, the electrolyte solution and light source were 0.2 mol/L Na_2SO_4 (pH 6.8) solution and 300 W xenon lamp, respectively. The working electrode was prepared as following: Catalyst powder (5 mg) was dispersed into 250 μL of isopropanol, 750 μL of H_2O and 20 μL 5% Nafion, and then sonicated for 30 min. 50 μL of the sample mixture was drop-coated onto FTO glass and dried at 60 °C to obtain working electrode.

All DFT calculations data was obtained by using the Quantum Espresso code [32]. The exchange-correlation energy was approximated by the generalized gradient approximation with the Perdew-Burke-Ernzerhof (PBE) functional. A 500 eV plane-wave kinetic energy cutoff was chosen. Geometry optimization was conducted with the Brillouin zone. The atomic positions were fully relaxed until a maximum energy difference and residual force on atoms, respectively. The vacuum slab of 15 Å was added to prevent the periodic interference of the unit cell.

Fig. 1a illustrated the basic synthetic procedure for *in-situ* growth of oxygen vacancies BiOCl on C_3N_5 nanosheets ($BiO_{1-x}Cl/C_3N_5$). As a new type of N-rich carbon nitride, C_3N_5 was chosen for its azo-linked structure, which has been proven to be ideal support to metal atoms. Additionally, it exhibited a enhanced visible-light response to provide photo-generated charge carriers [33]. Briefly, C_3N_5 nanosheets have been obtained by previously reported method [34], which were subsequently used as the *in-situ* growth substrate for $BiO_{1-x}Cl$ nanoparticles. The XRD pattern of C_3N_5 presented a main characteristic peak at 27° (Fig. 1b) [33]. The absence of a (100) peak, a specific feature of in-plane packing, suggests the distortion of C_3N_5 framework and the broadening of nanochannel distance between heptazine units due to azo (–N=N–) bridging linkage [33,35,36]. Also, both BiOCl and $BiO_{1-x}Cl$ were the tetragonal structure (JCPDS No 06-0249) (Fig. 1b and Fig. S2 in Supporting information). Notably, the oxygen vacancies treatment did not damage the crystalline structure of BiOCl. In $BiO_{1-x}Cl/C_3N_5$ heterojunction, the XRD peaks of $BiO_{1-x}Cl$ and C_3N_5 were clearly observed. As shown in Figs. 1c and d, $BiO_{1-x}Cl$ nanosheets were junctionalized with C_3N_5, confirming the formation of heterojunction structure. The spacing value of 0.275 nm was assigned to the $BiO_{1-x}Cl$ (110) plane (Fig. 1e), which showed an obvious boundary line with C_3N_5 (Fig. 1e). The uniformly distributed C, O, Bi, Cl, and N elements were the directional evidence for the tight heterojunction interface between $BiO_{1-x}Cl$ and C_3N_5 (Fig. 1f).

The defective nature of $BiO_{1-x}Cl/C_3N_5$ was verified *via* EPR spectra (Fig. 1g). Usually, the typical peak of vacancies at $g = 2.004$ was the signal for oxygen vacancies [37,38]. In comparison of BiOCl, $BiO_{1-x}Cl$ showed a stronger signal, indicating the successful introduction of oxygen vacancies [13]. Interestingly, the intensity of $BiO_{1-x}Cl/C_3N_5$ showed no obvious different to that of $BiO_{1-x}Cl$, probably due to the absence of the authentic bonding effect between $BiO_{1-x}Cl$ and C_3N_5 components. The result of Raman spectra further proved the existence of oxygen vacancies in $BiO_{1-x}Cl/C_3N_5$. As shown in Fig. 1h, BiOCl showed the characteristic peaks at 61, 143, 198, and 397 cm^{-1}, which were assigned to active modes of A_{1g}, A_{1g}, B_{1g}, and 2Eg, respectively [39]. These peaks of $BiO_{1-x}Cl$ were much weaker and slightly shifted to lower wavenumbers direction, suggesting the existence of abundant oxygen vacancies and metallic Bi [40]. The combination of C_3N_5 component did not change the oxygen vacancy concentration for the no obvious change peak intensities in $BiO_{1-x}Cl/C_3N_5$.

The XPS survey spectra of $BiO_{1-x}Cl/C_3N_5$ consisted of Bi, O, Cl, C, and N elements (Fig. S3 and Table S1 in Supporting information), suggesting the heterojunction structure of $BiO_{1-x}Cl/C_3N_5$. Fig. 2a presented the O 1s spectra. For $BiO_{1-x}Cl$, the peak at 529.8 eV was the crystal lattice O of $[Bi_2O_2]^{2+}$ crystal structure [41,42], and the peak at 531.9 eV originated from the oxygen vacancies [43,44]. The ~0.14 eV binding energy shifting between $BiO_{1-x}Cl$ and

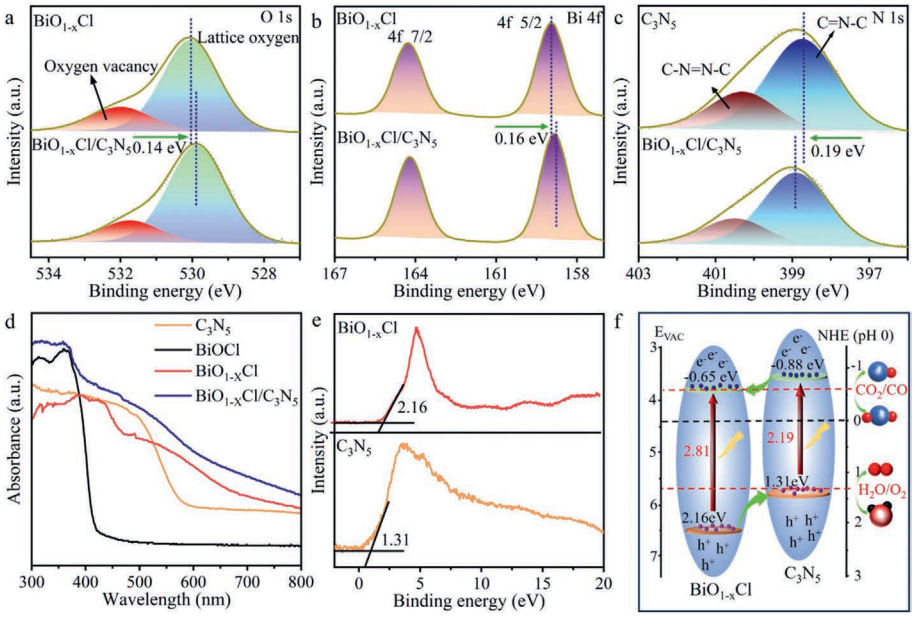


Fig. 2. O 1s (a), Bi 4f (b), and N 1s (c) XPS spectra of $BiO_{1-x}Cl/C_3N_5$. (d) UV–vis DRS spectra of C_3N_5, BiOCl, $BiO_{1-x}Cl$, and $BiO_{1-x}Cl/C_3N_5$. (e) Synergism illumination VB XPS (SI-VB XPS) spectra of C_3N_5 and $BiO_{1-x}Cl$. (f) Band structure alignments of $BiO_{1-x}Cl/C_3N_5$.

$BiO_{1-x}Cl/C_3N_5$ was from the interface interaction in $BiO_{1-x}Cl/C_3N_5$. Similar conditions were also be detected on C 1s and Cl 2p spectra (Figs. S4 and S5 in Supporting information). Referring to Fig. 2b, two peaks at 158.9 and 164.4 eV in $BiO_{1-x}Cl$ corresponded to Bi^{3+} $4f_{5/2}$ and $4f_{7/2}$, respectively. While in $BiO_{1-x}Cl/C_3N_5$, both peaks shifted down by ~0.16 eV for the increase in electron density of Bi atoms [45]. Correspondingly, the N 1s exhibited an opposite change. In $BiO_{1-x}Cl$, the peaks of two-coordinated (N2C) and three-coordinated (N3C) were detected at 398.5 and 399.8 eV, respectively (Fig. 2c) [33]. After constructing C_3N_5 component, these peaks shifted up by ~0.19 eV, indicating that the decrease in electron density in N nucleus. Thus, in $BiO_{1-x}Cl/C_3N_5$, the electrons shifted from the N atoms to Bi atoms. The similar situation was not detected in $BiOCl/C_3N_5$ counterpoint (Figs. S6 and S7 in Supporting information). Nevertheless, no peaks belong to Bi-N bond was detected in both Bi 4f (163.4 eV) and N 1s (398.18 eV) XPS spectra [46], which suggested in $BiO_{1-x}Cl/C_3N_5$ heterojunction, $BiO_{1-x}Cl$ and C_3N_5 was connected by the strong electrostatic effect [47,48]. In addition, with the introduction of high concentration oxygen vacancies, the band gap (E_g) of $BiO_{1-x}Cl$ was narrowed to 2.81 eV from 3.44 eV of BiOCl, a distinctive feature of defect-containing semiconductors (Fig. 2d and Fig. S8 in Supporting information) [49]. Similarly, the E_g of C_3N_5 was 2.19 eV. Moreover, the valence band potentials (E_{VB}) of C_3N_5 and $BiO_{1-x}Cl$ were determined by VB-XPS with light illumination (SI-VB XPS). The E_{VB} of C_3N_5 and $BiO_{1-x}Cl$ were 1.31 and 2.16 eV, respectively (Fig. 2e). Meanwhile, the corresponding the E_{CB} of C_3N_5 and $BiO_{1-x}Cl$ were −0.88 and −0.65 eV, respectively. Based on the above analysis, the band structures of $BiO_{1-x}Cl$ and C_3N_5 were depicted in Fig. 2f. It can be observed that $BiO_{1-x}Cl/C_3N_5$ met simultaneously the thermodynamic conditions for CO_2 reduction and H_2O oxidization.

Meanwhile, the weight ratios of $BiO_{1-x}Cl$ and C_3N_5 in $BiO_{1-x}Cl/C_3N_5$ heterojunction had great influence on the photocatalytic CO_2 conversion efficiency and CO selectivity. $BiO_{1-x}Cl/C_3N_5$ with 20 wt% $BiO_{1-x}Cl$ loading showed the highest CO production rate (Fig. S9 in Supporting information) and selectivity (Fig. 3a). The CO production rate of $BiO_{1-x}Cl/C_3N_5$ was 207.3 μmol g^{-1} h^{-1} with a 96.1 % selectivity (Fig. 3a), which was a 5.4-fold enhancement compared to that of $BiOCl/C_3N_5$. However, there was still a small amount of CO produced under the Ar atmosphere (Fig. S10 in Supporting information), which may be caused by the self-decomposition of C_3N_5 or added surfactants [50,51]. With sacrificial reagent addition, the CO evolution rate reached 1096.32 μmol g^{-1} h^{-1} (Fig. S11 in Supporting information). Furthermore, the obtained photocatalytic performance of $BiO_{1-x}Cl/C_3N_5$ was among the highest of reported works of Bi-based photocatalysis on CO_2 photoreduction to date (Fig. 3b and Table S2 in Supporting information). Meanwhile, $BiO_{1-x}Cl/C_3N_5$ also exhibited excellent photocatalytic stability and structure stability (Fig. 3c, Figs. S12 and S13 in Supporting information)

Furthermore, the isotopic labeling experiment was conducted by using $^{13}CO_2$ as a carbon source. As shown in Fig. 3d, the ^{13}CO peak at $m/z = 29$ and $^{13}COOH$ peak at $m/z = 46$ could be evidently detected in $BiO_{1-x}Cl/C_3N_5$ reaction system, confirming that CO should be produced from photocatalytic CO_2 reduction instead of impurities or pollutants [52–54]. Additionally, the oxidation products have also been explored through the $H_2{}^{18}O$ isotopic labeling experiment. As illustrated in Fig. S14 (Supporting information), ^{18}O ($m/z = 18$) and $^{18}O_2$ ($m/z = 36$) were simultaneously detected, indicating that the O_2 molecular product should be derived from water oxidation, which simultaneously provided electron/proton for CO_2 reduction into CO.

To investigate the origins of the photocatalytic performance, the electron dynamic behaviors were studied first. As shown in Fig. 3e, $BiO_{1-x}Cl/C_3N_5$ displayed the highest photocurrent density compared to $BiO_{1-x}Cl$ and $BiOCl/C_3N_5$, a result of the quicker charge transfer and separation rate after constructing the heterojunction. Meanwhile, similar conclusions were obtained from the electrochemical impedance spectroscopy (EIS). $BiO_{1-x}Cl/C_3N_5$ performed with the minimum radius (Fig. 3f), presenting that the fastest charge transfer rate and the lowest recombination ability of $BiO_{1-x}Cl/C_3N_5$ [55–57]. This was corroborated by the reduced photoluminescence (PL) intensity (Fig. 3g), where $BiO_{1-x}Cl/C_3N_5$ displayed significantly quenched signals compared to $BiO_{1-x}Cl$ and $BiOCl/C_3N_5$, highlighting suppressed electron-hole recombination [58–60]. To probe the specific charge transfer dynamics, the TRPL spectra were collected (Fig. 3h and Table S3 in Supporting information). The lifetime decay curve was well fitted by a biexponential

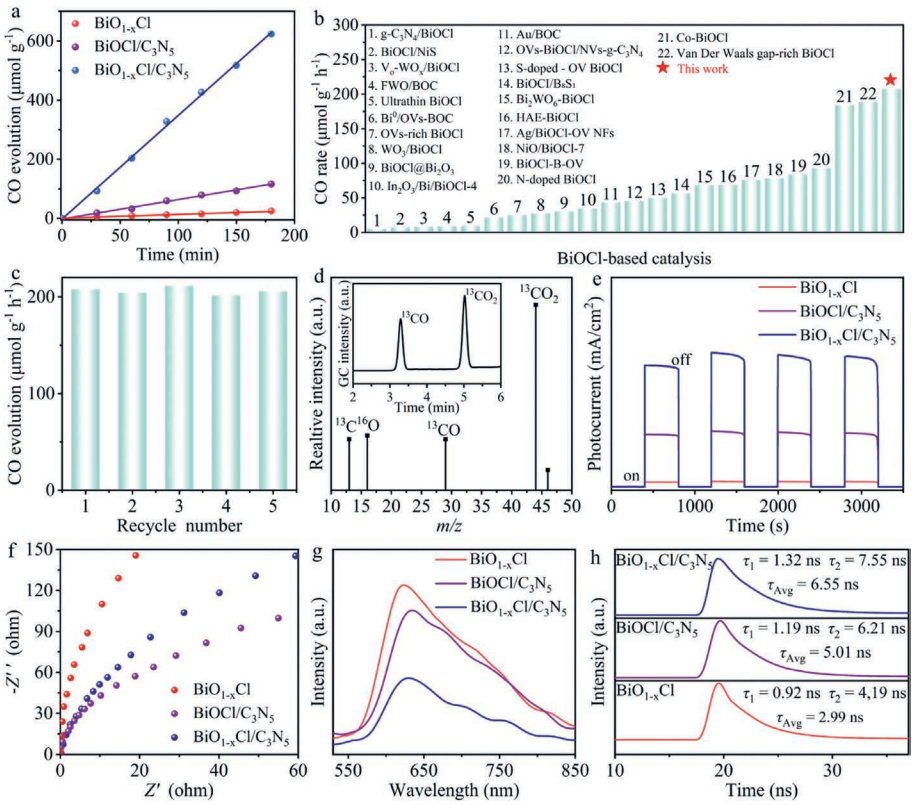


Fig. 3. (a) The photocatalytic CO_2 reduction performance of $BiO_{1-x}Cl/C_3N_5$. (b) Comparison of photocatalytic performance in CO_2 reduction of BiOCl-based photocatalysts. (c) The photostability of $BiO_{1-x}Cl/C_3N_5$. (d) ^{12}C isotope-labelled experiment result of $BiO_{1-x}Cl/C_3N_5$. *I-t* curve (e), EIS plot (f), PL (g), and time-resolved PL (h) of $BiO_{1-x}Cl/C_3N_5$.

kinetic function ($R^2 > 0.98$). The average carrier lifetime (τ_{avg}) of $BiO_{1-x}Cl/C_3N_5$ was 6.55 ns, which was much longer than these of $BiO_{1-x}Cl$ (2.92 ns) and $BiOCl/C_3N_5$ (5.01 ns), indicating the lower recombination ratios during the charge carrier transfer process under the excitation state [61,62]. Note that the $BiO_{1-x}Cl/C_3N_5$ showed a longer lifetime than $BiOCl/C_3N_5$, which maybe from the strong interface interaction, a main reason for the enhanced CO_2 photoreduction performance [63,64].

The effects of CO_2 absorption under darkness and light excitation on the structural evolution of $BiO_{1-x}Cl/C_3N_5$ heterojunction were explored by synchronous irradiation X-ray diffraction (SI-XRD) technique [65]. As depicted in Fig. 4a, the CO_2 adsorption on $BiO_{1-x}Cl/C_3N_5$ surface induced the evident shift of diffraction peaks toward the low d-spacing values, indicating that the shrinkage of crystalline structure owing to the electron deviated from $BiO_{1-x}Cl/C_3N_5$ to CO_2 molecules. Similar phenomena could also be observed in $BiOCl/C_3N_5$ (Fig. 4b) and $BiO_{1-x}Cl$ (Fig. 4c), respectively. Moreover, under light irradiation, the diffraction peaks of $BiO_{1-x}Cl/C_3N_5$ shifted to the high D-spacing direction, indicating that the formed intermediates induced the changes of crystalline structure in reverse. Similar phenomenon could be observed in the $BiOCl/C_3N_5$ with a smaller shift amplitude. However, no evident change could be observed on $BiO_{1-x}Cl$ under light irradiation, revealing its relatively poor capability for the formation of reaction intermediates.

The reaction intermediates during CO_2 photoreduction were determined by synchronous irradiation diffuse reflectance Fourier transform infrared spectroscopy (SI-DRIFTS). Under the darkness, compared to $BiO_{1-x}Cl$ and $BiOCl/C_3N_5$, $BiO_{1-x}Cl/C_3N_5$ presented a much higher CO_2 adsorption peak (~2300–2400 cm^{-1}) and H_2O adsorption peak (~1600–1700 cm^{-1}) (Fig. S15 in Supporting information), which revealed that the surface of $BiO_{1-x}Cl/C_3N_5$ was more favorable for the adsorption of CO_2 molecules [66]. Upon light irradiation on $BiO_{1-x}Cl/C_3N_5$, the peaks at 1504, 1531, and 1267 cm^{-1} assigned to $*CO_2$ intermediates could be evidently detected in Fig. 4d. Interestingly, the emergence of *COOH at 1698 cm^{-1} indicated the protonation of $*CO_2$ [67,68], which was the key for CO_2-to-CO conversion [69,70]. With increasing irradiation time, the peaks of *CO intermediates could be detected evidently. By comparison, the *CO peaks on $BiO_{1-x}Cl$ and $BiOCl/C_3N_5$ were much smaller, which confirmed the low CO production efficiencies of $BiO_{1-x}Cl$ and $BiOCl/C_3N_5$ (Figs. 4e and f).

Moreover, the dynamic evolutions of chemical bonds and electronic structures of $BiO_{1-x}Cl/C_3N_5$ during CO_2 reduction process were studied *via* synchronous irradiation X-ray photoelectron spectroscopy (SI-XPS) (Fig. 5 and Table S4 in Supporting information) [38,71,72]. After CO_2 absorption (Fig. 5a), the peaks at 289.3 and 286.2 eV in C 1s XPS spectrum can be indexed to $*CO_2$ and *CO intermediates originating from the adsorption and dissociation of CO_2 molecules [12]. Additionally, the slight peak at 290.8 eV indexed to carbonate species (CO_3^{2-}), which was consistent with the DRIFTS results. Simultaneously, two evident peaks at 166.7 and 166.0 eV in Bi 4f spectrum should be attributed to *CO and $*CO_2$ species on exposed Bi active sites (Fig. 5b). Under light irradiation, the intensities of CO_3^{2-} and $*CO_2$ peaks decreased evidently in C 1s region, while *CO peak increased obviously, indicating the dissociation of CO_2 molecules. Simultaneously, an evident decrease in Bi-CO_2* peak accompanying with increase in Bi-CO* peak was detected in Bi 4f spectrum. As illustrated in Fig. 5c, the O 1s peaks can be fitted into six peaks at 534.7, 533.3, 532.2, 531.9, 531.5, and 530.4 eV, which were assigned to H_2O, O=C, OH, O_v, O–C, and lattice O, respectively. Upon light irradiation, the intensities of H_2O and O=C peaks decreased evidently, while OH and O–C peaks increased obviously, revealing the dissociation of CO_2 and H_2O molecules over the $BiO_{1-x}Cl/C_3N_5$ surface. More importantly, all these chemical states and bond evolutions were dynam-

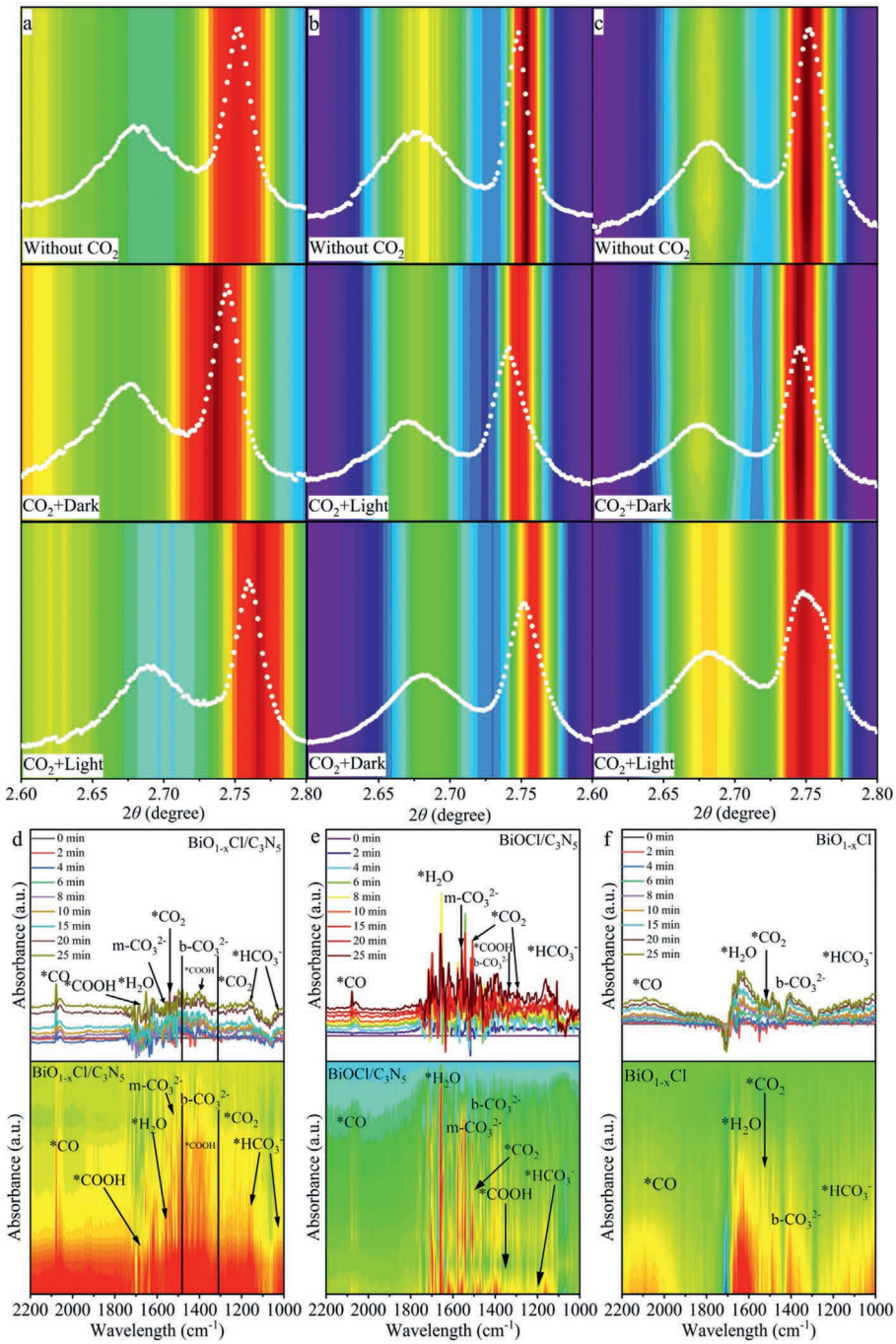


Fig. 4. The effect of CO_2 adsorption and light illimitation on the D-spacing evolution of $BiO_{1-x}Cl/C_3N_5$ (a), $BiOCl/C_3N_5$ (b), and $BiO_{1-x}Cl$ (c). Synchronous irradiation diffuse reflectance Fourier transform infrared spectroscopy (SI-DRIFTS) $BiO_{1-x}Cl/C_3N_5$ (d), $BiOCl/C_3N_5$ (e), and $BiO_{1-x}Cl$ (f).

ically reversible by controlling the light or dark conditions (Figs. 5d–f). Furthermore, Ar ion etching has been performed to remove the adsorbed CO_2 molecules, and all the related changes have been disappeared (Figs. 5g–i, Fig. S16 and Table S5 in Supporting information), further confirming the effects of adsorption and dissociation of CO_2 on the above chemical states and bond evolutions. For comparison, the related experiments of CO_2 adsorption have also been performed on $BiO_{1-x}Cl$ and $BiOCl/C_3N_5$, respectively. As illustrated in Figs. S17 and S18 (Supporting information), both $BiO_{1-x}Cl$ and $BiOCl/C_3N_5$ exhibited the relatively low CO_2 adsorption peaks compared with $BiO_{1-x}Cl/C_3N_5$, while no significant bond evolution could be detected, demonstrating the relatively poor CO_2 reduction capability. Therefore, the combination of C_3N_5 and $BiO_{1-x}Cl$ could effectively promote the adsorption of CO_2 molecules owing to the electron enrichment on Bi active sites. Under light illumination, the adsorbed $^*CO_2$ molecules were transformed into $^*CO$ intermediates with the transformation of high oxidation state Bi atoms to Bi^{3+}.

Furthermore, the surface charge distribution has been investigated by surface photovoltage (SPV) measurements. Fig. 5j confirmed that the light excitation induced the significant variations of surface potential, and the surface potential of $BiO_{1-x}Cl/C_3N_5$ was >138 mV, which was much higher than these of $BiOCl/C_3N_5$ (~74 mV) and $BiO_{1-x}Cl$ (~32.5 mV) (Figs. 5k and l). Therefore, $BiO_{1-x}Cl/C_3N_5$ effectively promoted the charge separation, photoinduced electron migration, and CO_2 adsorption.

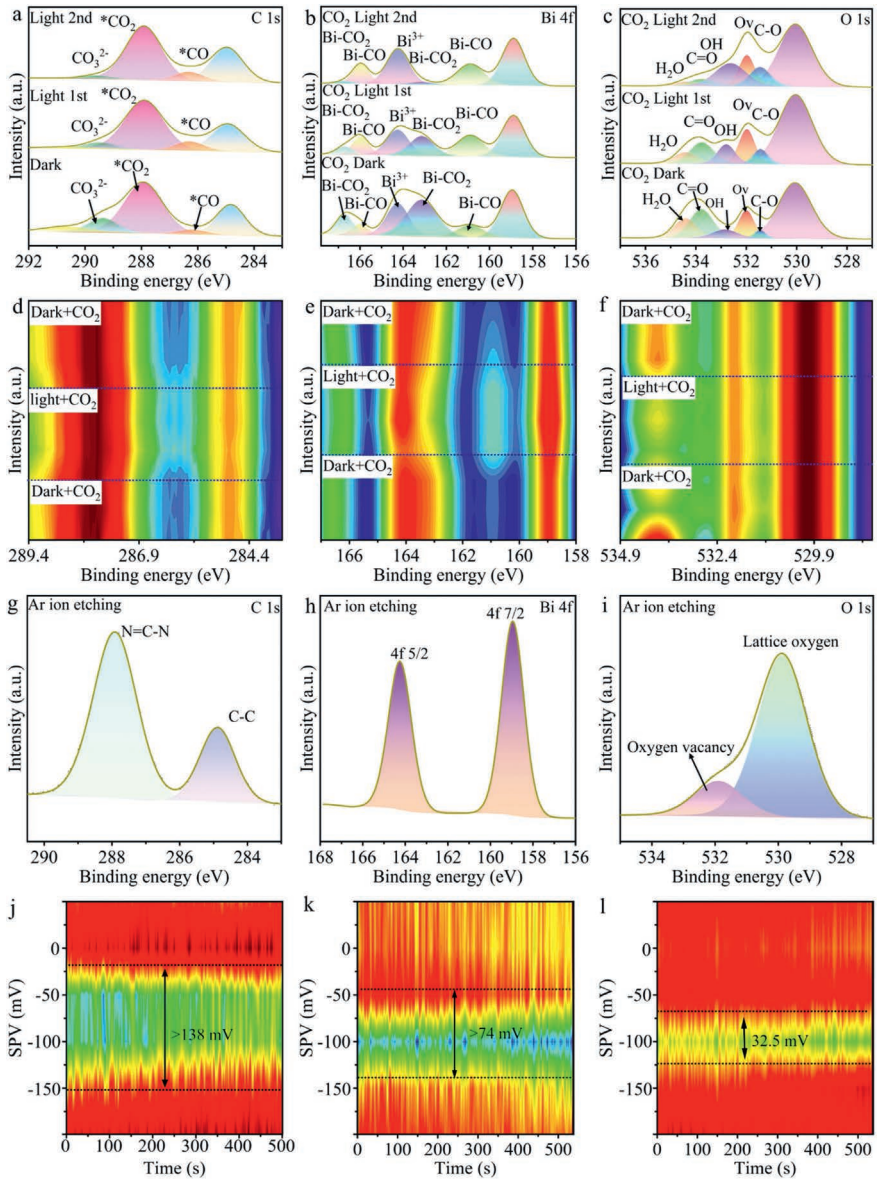


Fig. 5. High-resolution SI-XPS spectra of C 1s (a), Bi 4f (b), and O 1s (c) on $BiO_{1-x}Cl/C_3N_5$ with CO_2 adsorption under darkness and light irradiation. Effect of light illumination on the high-resolution SI-XPS spectra of C 1s (d), Bi 4f (e), and O 1s (f) of $BiO_{1-x}Cl/C_3N_5$ with CO_2 adsorption. C 1s (g), Bi 4f (h), and O 1s (i) of XPS spectra $BiO_{1-x}Cl/C_3N_5$ after Ar ion etching. SPV mapping of the surface potential distribution of $BiO_{1-x}Cl/C_3N_5$ (j), $BiOCl/C_3N_5$ (k), and $BiO_{1-x}Cl$ (l).

The radicals during CO_2 photoreduction are also the keys to unveil the reaction mechanism, which were investigated *via* the *in-situ* EPR spectra. As shown in Figs. 6a and b, the drastically reduced TEMPO signal and the increased DMPO–OH signal demonstrated that $BiO_{1-x}Cl/C_3N_5$ produced more photogenerated electrons and promoted more H_2O molecules dissociation under light illumination. When CO_2 was continually injected into $BiO_{1-x}Cl/C_3N_5$ system, the TEMPO signal showed no obvious changes during irradiation (Fig. 6c), suggesting that the photoinduced electrons were largely captured by CO_2 during photoreduction [73]. Also, even though CO_2 was injected, no any DMPO–OH signal was detected in $BiO_{1-x}Cl/C_3N_5$ system under dark, while switching to light illumination, DMPO–OH signal appeared and was higher with the illumination time prolonging (Fig. 6d), revealing the indispensable role of light in promoting water hydrolysis. Consequently, the CO_2 reduction process was promoted by the protons and photoinduced electrons ($CO_2 + 2e^- + 2H^+ \rightarrow CO + H_2O$). As a result, the ample photoinduced electrons and protons endowed $BiO_{1-x}Cl/C_3N_5$ favorable CO_2 photoreduction performance.

Temperature-programmed desorption (TPD) experiments were performed to study the interactions between $BiO_{1-x}Cl/C_3N_5$ and the reaction gases CO_2 and the product CO. The maximum CO_2 desorption temperature of $BiO_{1-x}Cl/C_3N_5$ was 400.8 °C, which was higher than these of $BiO_{1-x}Cl$ (346.1 °C) and $BiOCl/C_3N_5$ (323.7 °C), demonstrating the stronger interaction between CO_2 molecules and $BiO_{1-x}Cl/C_3N_5$ (Fig. S19 in Supporting information). In contrast, $BiO_{1-x}Cl/C_3N_5$ exhibited lower maximum CO desorption temperature (316.2 °C) compared to $BiO_{1-x}Cl$ (350.2 °C) and $BiOCl/C_3N_5$ (328.7 °C) (Fig. S20 in Supporting information), which illustrated that the CO molecules were more easier to release from $BiO_{1-x}Cl/C_3N_5$ [16,74]. Consequently, the CO_2-to-CO conversion was enhanced in $BiO_{1-x}Cl/C_3N_5$ system.

The interface interaction of $BiO_{1-x}Cl/C_3N_5$ was studied theoretically with an electron introduction. As depicted in Fig. 6e, compared to $BiOCl/C_3N_5$, the C_3N_5 component on $BiO_{1-x}Cl/C_3N_5$ deformed obviously with a deformation energy of −2.26 eV, almost twice that of $BiOCl/C_3N_5$ (−1.19 eV). The obvious deformation energy difference may originate from the amplified interfacial inter-

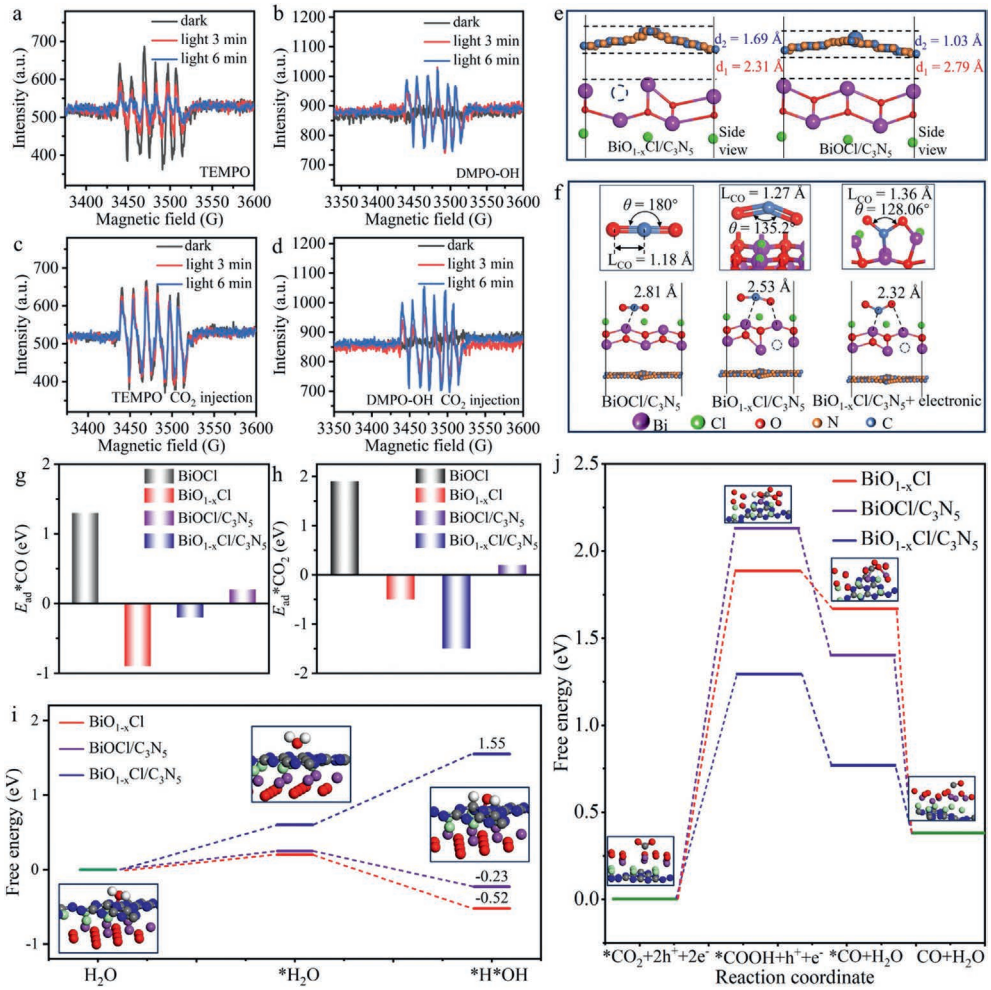


Fig. 6. *In-situ* EPR patterns of TEMPO (a) and DMPO–OH (b) before and after light illumination on $BiO_{1-x}Cl/C_3N_5$. *In-situ* EPR patterns of TEMPO (c) and DMPO–OH (d) before and after light illumination on $BiO_{1-x}Cl/C_3N_5$ with CO_2 injection. (e) Structure models of $BiO_{1-x}Cl/C_3N_5$ and $BiOCl/C_3N_5$ after optimization. (f) The optimized structure models of $BiO_{1-x}Cl/C_3N_5$ and $BiOCl/C_3N_5$ after CO_2 adsorption. The adsorption energies of $^*CO$ (g) and $^*CO_2$ (h) intermediates on $BiO_{1-x}Cl/C_3N_5$ surface. Standard Gibbs free energy profile of H_2O molecular dissociation (i) and CO_2 molecular reduction (j) on $BiO_{1-x}Cl/C_3N_5$ surface.

action. Additionally, as a result of the stronger interfacial interaction, the distance between $BiO_{1-x}Cl$ and C_3N_5 (2.31 Å) was shorter in comparison to that in $BiOCl/C_3N_5$ (2.79 Å), and the binding energy E_b in $BiO_{1-x}Cl/C_3N_5$ (−4.03 eV) was much smaller than that in $BiOCl/C_3N_5$ (−2.91 eV), showing the stronger interfacial interaction between C_3N_5 and $BiO_{1-x}Cl$ (Fig. S21 in Supporting information).

Herein, the dynamic CO_2 conversion on $BiO_{1-x}Cl/C_3N_5$ was simulated. To model CO_2 adsorption on $BiO_{1-x}Cl/C_3N_5$, a CO_2 molecule was placed above $BiO_{1-x}Cl$s side. Five adsorption sites were designed (Fig. S22 in Supporting information), including Bi atom, Bi atom adjected O_v (Bi-O_v), O atom, O_v site, and Cl atom. Also, adsorption energy (E_{ads}) was calculated as $E_{ads} = E_{CO_2@BiO_{1-x}Cl/C_3N_5} - E_{BiO_{1-x}Cl/C_3N_5} - E_{CO_2}$, where $E_{CO_2@BiO_{1-x}Cl/C_3N_5}$ was the CO_2 adsorption energy on $BiO_{1-x}Cl/C_3N_5$. As a result, $E_{BiO_{1-x}Cl/C_3N_5}$ and E_{CO_2} referred to the energies of $BiO_{1-x}Cl/C_3N_5$ and a CO_2 molecule, respectively. The E_{ads} values for Bi, Bi-O_v, O, O_v, and Cl were −0.24, −0.32, −0.02, −0.14, and 0.15 eV, respectively. The Bi-O_v site was the most suitable site towards CO_2 adsorption.

In order to identify the dynamic evolution of CO_2 molecule on Bi-O_v site, one electron was introduced into the calculation models. As illustrated in Fig. 6f, after geometry optimization, the CO_2 molecule adsorbed on Bi-O_v site induced the deformation of $BiO_{1-x}Cl$ and C_3N_5 components in the interface, while there was no so obvious deformation in $BiOCl/C_3N_5$, implying the bigger interaction strength of CO_2 on $BiO_{1-x}Cl/C_3N_5$. The CO_2 molecule adsorbed on $BiOCl/C_3N_5$ showed no obvious deformation with a distance of 2.81 Å on BiOCl layer. While on $BiO_{1-x}Cl/C_3N_5$, the distance between CO_2 molecule and $BiO_{1-x}Cl$ layer was decreased to 2.53 Å. The CO_2 molecule distorted with O=C=O angle of 135.12°, and C and O atoms formed Bi–C and Bi–O bonds with Bi atoms. By introducing an electron, the C–O bond in Bi–O–C–Bi group was stretched from 1.18 Å to 1.33 Å and the O=C=O angle was reduced to 128.06°, which indicated the approaching dissociation of CO_2 molecule [16]. In summary, $BiO_{1-x}Cl/C_3N_5$ enhanced the interaction between exposed Bi atoms and CO_2 molecules and then destructed the linear structure of CO_2 molecules, thereby achieving the efficient activation of CO_2 molecules.

From the energy aspect, the adsorption energy of CO_2 molecules on $BiO_{1-x}Cl/C_3N_5$ surface was bigger compared to these on $BiOCl/C_3N_5$ and $BiO_{1-x}Cl$ (Fig. 6g), revealing that oxygen vacancies in $BiO_{1-x}Cl/C_3N_5$ enhanced the interaction between electrons and CO_2. While the adsorption energies (E_{ad}*CO) of $BiO_{1-x}Cl/C_3N_5$ was smaller than that of $BiOCl/C_3N_5$, which demonstrated that $^*CO$ intermediates on $BiO_{1-x}Cl/C_3N_5$ was easier to release (Fig. 6h). Moreover, the free energy of H_2O dissociation on $BiO_{1-x}Cl/C_3N_5$ was calculated to be *ca.* −0.52 eV, which was smaller than these of $BiOCl/C_3N_5$ (1.55 eV) and $BiO_{1-x}Cl$ (−0.23 eV) (Fig. 6i), confirm-

ing that the $BiO_{1-x}Cl/C_3N_5$ accelerated H_2O dissociation and facilitated proton-feeding [75]. Besides, the *H acquisition ability of $BiO_{1-x}Cl/C_3N_5$ provided the enough *H for the formation of *COOH intermediates, thereby enhancing the photocatalytic reduction process [76].

Gibbs free energies of the CO_2 reduction elementary steps were performed (Fig. 6j). Generally, in CO_2-to-CO conversion process, the *COOH and *CO intermediates were the keys [77]. The *COOH intermediates was first formed on Bi sites *via* the process of $*CO_2 + H^+ + e^- \rightarrow *COOH$, which was considered as the rate-determining step for the CO_2-to-CO conversion [78]. The smallest *COOH formation energy on $BiO_{1-x}Cl/C_3N_5$ was from the compact heterojunction structure and optimized electron states. In the second hydrogenation step, *COOH was converted into *CO specie and remained absorbed on the catalyst surface. Owing to the negative energy for *CO intermediates desorption, the adsorbed CO molecules were easily to form product CO rather than the products involved with more than two-electron processes (such as CH_3OH and CH_4). From the above analysis, the CO_2 reduction produced CO as the final product on $BiO_{1-x}Cl/C_3N_5$.

Based on the above demonstrations, a potential mechanism has been proposed to clarify the charge separation, electron transport, structure and bond evolutions over $BiO_{1-x}Cl/C_3N_5$ during the photocatalytic CO_2 reduction. Firstly, the strong interfacial interaction enriched the electrons on Bi sites, facilitating the CO_2 molecules adsorption. Subsequently, the strong electron-attracting ability of absorbed CO_2 molecules pushed up the oxidation state of Bi atoms and the shrinkage of $BiO_{1-x}Cl/C_3N_5$ crystalline structures. Upon light illumination, the photoinduced electron further strengthened the interaction between CO_2 molecule and Bi active site, which efficiently destroyed the linear structure of CO_2 molecule, facilitating $*CO_2$ to form *COOH intermediates. Then, *COOH was further reduced to *CO *via* reacting with proton and photoinduced electron. Finally, the *CO desorbed and formed CO gas, accompanying with the restoration of the crystalline structures of $BiO_{1-x}Cl/C_3N_5$. Thus, the dynamic structure and chemical state evolutions of $BiO_{1-x}Cl/C_3N_5$ during photoreaction were the main reasons for the high CO_2-to-CO conversion.

In summary, using $BiO_{1-x}Cl/C_3N_5$ as a model photocatalyst in CO_2 reduction, we revealed the strong relationship between dynamic structure evolution and photocatalytic performance. More specifically, owing to the combination of C_3N_5 and $BiO_{1-x}Cl$, the interface electron enriched on Bi sites, which effectively promoted the adsorption of CO_2 molecules. Under light illumination, at the joint action of photoinduced electrons and protons, the adsorbed structure-twisted CO_2 molecules were transformed into *CO intermediates, leading to restoration of crystalline structure and valence state of Bi active sites. As expected, $BiO_{1-x}Cl/C_3N_5$ photocatalyst exhibited excellent CO_2-to-CO conversion activity with an CO evolution rate of 207.3 $\mu mol\ g^{-1}\ h^{-1}$. These findings might help to reveal the origin of photocatalytic performance of catalysts during CO_2 conversion and provide a new insight to design efficient and stable photocatalysts for CO_2 reduction.

CRediT authorship contribution statement

Zhilei Chen: Writing – original draft, Visualization, Validation, Software, Resources, Methodology, Investigation, Formal analysis, Data curation. **Zhaoxia Li:** Writing – original draft, Validation, Software, Resources, Methodology, Investigation, Formal analysis, Data curation. **Yunjiang Yu:** Writing – original draft, Validation, Resources, Methodology, Investigation, Formal analysis, Data curation. **Mingdeng Xiang:** Writing – original draft, Resources, Methodology, Investigation, Formal analysis. **Cheng Ding:** Writing – review & editing, Supervision, Software, Resources, Project administration, Methodology, Investigation, Funding acquisition, Formal analysis, Data curation. **Entian Cui:** Writing – original draft, Validation, Software, Resources, Project administration, Methodology, Investigation, Funding acquisition, Formal analysis, Data curation. **Jizhou Jiang:** Writing – review & editing, Visualization, Validation, Supervision, Software, Resources, Project administration, Methodology, Investigation, Funding acquisition, Formal analysis, Data curation, Conceptualization.

Declaration of competing interest

The authors declare that they have no known competing financial interests or personal relationships that could have appeared to influence the work reported in this paper.

Acknowledgments

This work is supported by the National Natural Science Foundation of China (No. 62004143), the Key Project of Scientific Research Plan of Hubei Provincial Department of Education (No. D20241501), the Major Project of Natural Science Foundation of Jiangsu Universities, China (No. 23KJA150010), the Innovation Project of Engineering Research Center of Phosphorus Resources Development and Utilization of Ministry of Education (No. LCX202404), and the Major Project of Natural Science Foundation of Jiangsu Universities, China (No. 23KJA150010).

Supplementary materials

Supplementary material associated with this article can be found, in the online version, at doi:10.1016/j.cclet.2025.112313.

References

[1] D. Wen, N. Wang, J. Peng, et al., J. Mater. Sci. Technol. 226 (2025) 93–108.
[2] H. Zhou, W. Ye, J. Jiang, et al., Carbon Lett. 34 (2024) 1569–1591.
[3] P. Huang, J. Huang, S.A. Pantovich, et al., J. Am. Chem. Soc. 140 (2018) 16042–16047.
[4] H. Yue, Z. Jinfeng, R. Olim, et al., Comp. Funct. Mater. 1 (2025) 20250103.
[5] J. Tang, C. Guo, T. Wang, et al., Carbon Neutralization 3 (2024) 557–583.
[6] Z. Sun, N. Talreja, H. Tao, et al., Angew. Chem. Int. Ed. 57 (2018) 7610–7627.
[7] Y. Wang, J. Sheng, X. Zhao, et al., Chin. Chem. Lett. 34 (2023) 107967.
[8] H. Lu, Q. Hao, T. Chen, et al., Appl. Catal. B: Environ. 237 (2018) 59–67.
[9] J. Deng, D. Xu, J. Zhang, et al., J. Mater. Sci. Technol. 180 (2024) 150–159.
[10] A. Helal, F.A. Harraz, A.A. Ismail, et al., Appl. Catal. B: Environ. 213 (2017) 18–27.
[11] F. Huang, Y. Liu, F. Wang, et al., Sci. China Mater. 68 (2025) 1561–1569.
[12] Y. Lan, Y. Zhang, X. Huang, et al., Angew. Chem. Int. Ed. 63 (2024) e202407736.
[13] H. Li, J. Li, Z. Ai, et al., Angew. Chem. Int. Ed. 57 (2018) 122–138.
[14] M. Guan, C. Xiao, J. Zhang, et al., J. Am. Chem. Soc. 135 (2013) 10411–10417.
[15] S. Wang, Q. Chen, T. Gao, et al., J. Mater. Sci. Technol. 215 (2025) 1–14.
[16] Y. Shi, J. Li, C. Mao, et al., Nat. Commun. 12 (2021) 5923.
[17] T. Peng, Y. Wang, C.L. Dong, et al., Nano-Micro Lett. 17 (2025) 223.
[18] K. Xu, L. Wang, H. Feng, et al., J. Mater. Sci. Technol. 77 (2021) 217–222.
[19] Z.Q. Li, X.H. Chen, T. Li, et al., Appl. Surf. Sci. 615 (2023) 156283.
[20] C. Tan, L. Ai, L. Wang, et al., ACS Appl. Nano Mater. 6 (2023) 21216–21225.
[21] Y. Wu, B. Yuan, M. Li, et al., Chem. Sci. 6 (2015) 1873–1878.
[22] M. Guo, Z. Zhou, S. Yan, et al., Sci. Rep. 10 (2020) 18401.
[23] C. Wang, N. Liu, X. Zhao, et al., J. Mater. Sci. Technol. 164 (2023) 188–197.
[24] J. Liu, H. Wang, M.J. Chang, et al., Sep. Purif. Technol. 301 (2022) 121953.
[25] K. Su, L. Zheng, M. Liu, et al., Small 20 (2024) e2405551.
[26] Y. Xin, J. Tian, X. Xiong, et al., Adv. Mater. 37 (2025) e2417589.
[27] D. Zu, Y. Ying, Q. Wei, et al., Angew. Chem. Int. Ed. 63 (2024) e202405756.
[28] D. Wen, N. Wang, J. Peng, et al., Chin. J. Catal. 69 (2025) 58–74.
[29] E. Cui, Y. Lu, J. Jiang, et al., Chin. J. Catal. 59 (2024) 126–136.
[30] C. Yuan, H. Yin, J. Li, et al., Nat. Commun. 16 (2025) 6607.
[31] S. Cheng, Z. Sun, K.H. Lim, et al., ACS Appl. Nano Mater. 6 (2023) 3608–3617.
[32] P. Giannozzi, S. Baroni, N. Bonini, et al., J. Phys. Condens. Matter. 21 (2009) 395502.
[33] P. Kumar, E. Vahidzadeh, U.K. Thakur, et al., J. Am. Chem. Soc. 141 (2019) 5415–5436.
[34] J. Zhang, Z. Li, J. He, et al., ACS Catal. 13 (2022) 785–795.
[35] R.C. Pawar, S. Kang, J.H. Park, et al., Sci. Rep. 6 (2016) 31147.
[36] D. Liu, S. Chen, Y. Zhang, et al., Appl. Catal. B: Environ. 333 (2023) 122805.
[37] X. Zhao, K. Gao, S. Xue, et al., Chin. Chem. Lett. 36 (2025) 110309.
[38] Y. Zhang, Z. Xu, Q. Wang, et al., Appl. Catal. B: Environ. 299 (2021) 120679.
[39] S. Weng, B. Chen, L. Xie, et al., J. Mater. Chem. A 1 (2013) 3068.
[40] H. Li, J. Shi, K. Zhao, et al., Nanoscale 6 (2014) 14168–14173.

[41] Z. Wu, M.-C. Chong, S. Zhang, et al., Sci. China Chem. 67 (2024) 1839–1864.
[42] S. Cheng, Z. Sun, K.H. Lim, et al., ACS Catal. 13 (2023) 7221–7229.
[43] L. Wang, R. Wang, T. Qiu, et al., Nano Lett. 21 (2021) 10260–10266.
[44] X. Zhao, Y. Xia, H. Li, et al., Appl. Catal. B: Environ. 297 (2021) 120426.
[45] C. Liu, Y. Ren, Z. Wang, et al., J. Colloid Interface Sci. 607 (2022) 423–430.
[46] X. Zhang, L. Ai, C. Tan, et al., Sep. Purif. Technol. 355 (2025) 129542.
[47] C. Zhou, Z. Jie, S. Xue, et al., Sci. Sin. Chim. 53 (2023) 1588–1599.
[48] J. Wu, Y. Chen, L. Zhang, et al., J. Ind. Eng. Chem. 129 (2024) 424–434.
[49] P. Makuła, M. Pacia, W. Macyk, J. Phys. Chem. Lett. 9 (2018) 6814–6817.
[50] Y. Zhang, D. Yao, B. Xia, et al., ACS Energy Lett. 7 (2022) 1611–1617.
[51] J. Zhang, T. Yuan, H. Wan, et al., Sci. China Chem. 60 (2017) 1546–1553.
[52] S. Wang, J. Henzie, B. Jiang, et al., Nat. Commun. 14 (2023) 2534.
[53] J. Di, X. Zhao, C. Lian, et al., Nano Energy 61 (2019) 54–59.
[54] S. Li, F. Chen, S. Chu, et al., Small 19 (2022) 2203559.
[55] Z. Li, Y. Zhou, Y. Zhou, et al., Nat. Commun. 14 (2023) 5742.
[56] X. Liu, G. Dawson, K. Papadikis, et al., J. Ind. Eng. Chem. 145 (2025) 561–576.
[57] S. Li, M. Cai, C. Wang, et al., J. Mater. Sci. Technol. 123 (2022) 177–190.
[58] W. Cai, Y. Tanaka, X. Zhu, et al., Nano Res. 17 (2024) 7027–7038.
[59] A. Amari, H.S.S. Aljibori, Z. Algarni, et al., J. Ind. Eng. Chem. 140 (2024) 599–616.
[60] B. Wang, H. Chen, F. Huang, et al., Appl. Catal. B: Environ. 374 (2025) 125394.
[61] B. Wang, W. Zhang, G. Liu, et al., Adv. Funct. Mater. 32 (2022) 2202885.
[62] J.I. Khan, F.H. Isikgor, E. Ugur, et al., ACS Energy Lett. 6 (2021) 4155–4164.
[63] Z. Zhou, J. Wang, M. Reheimujiang, et al., J. Mater. Sci. Technol. 213 (2025) 241–251.
[64] F. Xu, K. Meng, B. Cheng, et al., Nat. Commun. 11 (2020) 4613.
[65] Y. Wang, C. Liu, Y. Ren, et al., J. Am. Chem. Soc. 144 (2022) 5335–5341.
[66] B. Wang, H. Chen, W. Zhang, et al., Adv. Mater. 36 (2024) e2312676.
[67] X. Sun, T. Xian, C. Sun, et al., J. Mater. Sci. Technol. 228 (2025) 256–268.
[68] H. Li, C. Gao, G. Yang, et al., Chin. Chem. Lett. 36 (2025) 110547.
[69] J. Zhang, J. Fu, K. Dai, J. Mater. Sci. Technol. 116 (2022) 192–198.
[70] Z. Yao, H. Cheng, Y. Xu, et al., Nat. Commun. 15 (2024) 9881.
[71] W. Yan, Y. Zhang, Y. Bi, Angew. Chem. Int. Ed. 63 (2024) e202316459.
[72] W. Weng, Z. Lin, H. Zhang, et al., JACS Au 3 (2023) 3391–3399.
[73] Y. He, S. Dai, J. Sheng, et al., Proc. Natl. Acad. Sci. U. S. A. 121 (2024) e2322107121.
[74] Y. Shi, G. Zhan, H. Li, et al., Adv. Mater. 33 (2021) 2100143.
[75] S. Chen, Z. Zhang, W. Jiang, et al., J. Am. Chem. Soc. 144 (2022) 12807–12815.
[76] L. Wang, T. Yang, B. Feng, et al., Chin. J. Catal. 54 (2023) 265–277.
[77] S. Hu, P. Qiao, X. Yi, et al., Angew. Chem. Int. Ed. 62 (2023) e202304585.
[78] S. Wang, J. Wang, Y. Wang, et al., ACS Catal. 14 (2024) 10760–10788.